Influence of gravity waves on the Martian atmosphere: General circulation modeling

Alexander S. Medvedev,[1] Erdal Yiğit,[2] Paul Hartogh,[1] and Erich Becker[3]

Received 18 April 2011; revised 20 July 2011; accepted 20 July 2011; published 18 October 2011.

[1] Our recently developed nonlinear spectral gravity wave (GW) parameterization has been implemented into a Martian general circulation model (GCM) that has been extended to ~130 km height. The simulations reveal a very strong influence of subgrid-scale GWs with non-zero phase velocities in the upper mesosphere (100–130 km). The momentum deposition provided by breaking/saturating/dissipating GWs of lower atmospheric origin significantly decelerate the zonal wind, and even produce jet reversals similar to those observed in the terrestrial mesosphere and lower thermosphere. GWs also weaken the meridional wind, transform the two-cell meridional equinoctial circulation to a one-cell summer-to-winter hemisphere transport, and modify the zonal-mean temperature by up to ±15 K. Especially large temperature changes occur over the winter pole, where GW-altered meridional circulation enhances both "middle" and "upper" atmosphere maxima by up to 25 K. A series of sensitivity tests demonstrates that these results are not an artefact of a poorly constrained GW scheme, but must be considered as robust features of the Martian atmospheric dynamics.

Citation: Medvedev, A. S., E. Yiğit, P. Hartogh, and E. Becker (2011), Influence of gravity waves on the Martian atmosphere: General circulation modeling, *J. Geophys. Res.*, *116*, E10004, doi:10.1029/2011JE003848.

1. Introduction

[2] Being an intrinsic feature of convectively stably stratified fluids, gravity waves (GWs) play an important role in vertical coupling between atmospheric layers by redistributing energy and momentum, and affecting the transport of heat and constituents. There is a growing evidence that small-scale disturbances interpreted as GWs are not only continuously present in the atmosphere of Mars, but they are particularly strong [*Hinson et al.*, 1999; *Tolson et al.*, 1999, 2002; *Creasey et al.*, 2006a, 2006b; *Fritts et al.*, 2006; *Withers*, 2006]. Very large GW amplitudes inferred from radio occultation, descent, and accelerometer data agree well with the current knowledge of the meteorology of the Martian lower atmosphere, where large terrain irregularities, vertical wind shears, instabilities in weather systems, and volatile convection constitute very strong excitation mechanisms of GWs.

[3] Larger than on Earth, GW amplitudes imply a very significant dynamical role of these waves in the Martian atmosphere. *Fritts et al.* [2006] inferred from aerobraking density measurements that GW momentum deposition is of the order of 1000 m s^{-1} sol^{-1} at ~100 km. Using one-dimensional simulations, *Parish et al.* [2009] demonstrated that vertically propagating small-scale GWs can reach thermospheric heights, and create an appreciable body force of several thousands of m s^{-1} sol^{-1} at those altitudes. *Heavens et al.* [2010] discovered a possible GW saturation signal in convective instability or near-instability of temperature profiles obtained from Mars Climate Sounder onboard Mars Reconnaissance Orbiter. They estimated that the associated GW "drag" can be as large as 4500 m s^{-1} sol^{-1} at 0.1 Pa level (~80 km).

[4] Paradoxically, current Martian general circulation models (GCMs) are apparently able to reproduce the observed temperature fields without involving GW effects, at least up to 80–100 km. This can partly be explained by the large amplitudes of the resolved-scale eddies (tides, stationary and planetary waves), and, thus, of their Eliassen-Palm (EP) flux divergences. It is quite different from Earth, where the circulation in the entire mesosphere and lower thermosphere (MLT) is driven mainly by dissipating small-scale GWs. How can the apparent lack of dynamical influence of GWs in the Martian middle atmosphere be reconciled with their strong generation and large amplitudes? One hint toward resolving this dichotomy was provided by the results of *Kuroda et al.* [2009] who showed that larger-scale GWs contribute almost equally with tides and planetary waves to the enhancement of the meridional circulation during dust storms, and, thus, to the warmings over the winter poles at 60–70 km.

[5] The dynamical influence of small-scale GWs on the atmosphere of Mars was studied using GCMs in the past [*Barnes*, 1990; *Théodore et al.*, 1993; *Joshi et al.*, 1995, 1996; *Collins et al.*, 1997]. They all employed parameterizations of

[1]Max Planck Institute for Solar System Research, Katlenburg-Lindau, Germany.
[2]Center for Space Environment Modeling, University of Michigan, Ann Arbor, Michigan, USA.
[3]Leibniz Institute of Atmospheric Physics, Kühlungsborn, Germany.

0148-0227/11/2011JE003848

subgrid-scale GWs to show that the waves can be important near the edge of the westerly jet in the winter hemisphere, where the magnitudes of GW-induced drag vary from tens to hundreds of m s^{-1} sol^{-1}. These modeling studies had several features in common: (1) the upper boundaries of the associated model domains were limited to 80–100 km; (2) they all utilized Lindzen-type parameterizations (that is, assuming non-interacting harmonics and sudden onset of instabilities); (3) they considered only topographically generated harmonics with horizontal phase speed $c = 0$ (except *Théodore et al.* [1993] who included also waves with $c = \pm 20$ m s^{-1}). "Orographic" GW parameterizations are now routinely used in some Martian GCMs [*Forget et al.*, 1999; *Hartogh et al.*, 2005], however, they contribute only ≈10% of the EP flux divergence associated with resolved eddies [*Medvedev and Hartogh*, 2007].

[6] On the other hand, GW harmonics with nonzero phase velocities, that is $c \neq 0$, are known to be very important in the terrestrial MLT. The momentum they deposit to the mean flow reverses both easterly and westerly solstitial stratospheric jets, drives the meridional pole-to-pole circulation, and reverses the meridional temperature gradients near the mesopause. Since comprehensive terrestrial GCMs covering the MLT and the regions above are currently still unable to resolve small-scale waves, most of them employ one or another parameterization of subgrid-scale GW effects. Martian GCMs have been extended to thermospheric heights [*González-Galindo et al.*, 2009a], or specialized terrestrial thermospheric models have been adapted to Mars [*Bougher et al.*, 2004, 2006, 2008, 2011]. None of them, however, uses parameterizations for GWs with $c \neq 0$.

[7] Recently, we have developed an extended spectral nonlinear GW scheme suitable for both lower and upper planetary atmospheres. It consistently accounts for the refraction of waves by the mean wind and temperature, nonlinear interactions, breaking, and damping by various dissipative mechanisms [*Yiğit et al.*, 2008]. The scheme was extensively tested with a terrestrial GCM extending from the troposphere to upper thermospheric altitudes [*Yiğit et al.*, 2009; *Yiğit and Medvedev*, 2009, 2010]. The simulations demonstrated a significant dynamical and thermal role of internal GWs of lower atmospheric origin not only in the MLT, but in the thermosphere above the turbopause as well.

[8] The use of the scheme also improved the simulated fields when compared against the existing Earth observations. When the parameterization was applied to the wind and temperature distributions from the Mars Climate Database (MCD) (that is based on the output of the Laboratoire de Météorologie Dynamique (LMD) GCM [*González-Galindo et al.*, 2009a]), the calculations revealed an extremely large drag in the Martian thermosphere at all seasons [*Medvedev et al.*, 2011]. Such drag is clearly incompatible with the MCD wind, thus indicating that a substantial part of the momentum and energy budgets associated with GWs is probably missing in the GCM. Further analysis showed that the enormously large torque provided by GWs to the mean flow above 100 km resulted almost entirely from the MCD zonal wind being excessively easterly (retrograde).

[9] In this paper, we quantify the role of GWs in the Martian atmosphere by implementing the spectral nonlinear GW scheme of *Yiğit et al.* [2008] into our Martian GCM [*Hartogh et al.*, 2005; *Medvedev and Hartogh*, 2007], and by performing fully interactive simulations. The parameterization and the GCM are outlined in sections 2 and 3, correspondingly. Observational data that allow to constrain the GW scheme are discussed in section 4. Results of simulations with and without accounting for GW effects are presented in section 5, while the sensitivity of the results to GW source variations and to the accounting for GW radiative damping are described in sections 6 and 7. Section 8 contains a brief summary and conclusions.

2. Gravity Wave Parameterization

[10] The extended gravity wave scheme has been fully described in the work of *Yiğit et al.* [2008]. It solves the equation for the vertical propagation of horizontal momentum fluxes (per unit mass) $F_j = \overline{u'w'_j}$ associated with a harmonic j in the incident spectrum:

$$F_j(z) = F_j(z_0)\rho(z_0)\rho^{-1}(z)\exp\{-\int_{z_0}^{z}[\beta^j_{mol} + \beta^j_{non}]dz'\}. \quad (1)$$

In the above equation, u' and w' are the horizontal and vertical components of wind perturbations, the overline denotes an appropriate averaging over subgrid scales, ρ is the neutral mass density, z_0 is the reference (or source) level. β^j_{mol} and β^j_{non} are the vertical damping rates due to molecular viscosity and thermal conduction, and due to the effects of nonlinear saturation and breaking, respectively. For conservative propagation $\beta^j_{mol} = \beta^j_{non} = 0$, no divergence of the flux ρF_j takes place, and, thus, the net effect of the harmonic on the mean flow is zero. The vertical damping rate due to molecular viscosity and thermal conduction (assuming that the Prandtl number is equal to unity), β^j_{mol}, has the form [*Yiğit et al.*, 2008; *Vadas and Fritts*, 2005, and references therein]

$$\beta^j_{mol} = \frac{2\nu_{mol}N^3}{k_h|c_j - \overline{u}|^4}, \quad (2)$$

where N is the buoyancy frequency, $k_h = |\mathbf{k_h}|$ and c_j are the horizontal wave number and phase speed of the harmonic j, respectively, $\overline{u}(z)$ is the mean horizontal wind, ν_{mol} is the kinematic molecular viscosity. β^j_{non} describes the dissipation of the harmonic j caused by nonlinear interactions with other waves in the spectrum. This dissipation is the result of instabilities on scales shorter than the vertical wavelength of a given harmonic. If the spectrum consists of a single harmonic, the wave interacts nonlinearly with itself referred to as "self-interaction", and the corresponding β^j_{non} describes the well-known Hodges-Lindzen breaking due to convective instability but at ~70% ($1/\sqrt{2}$) amplitude compared to the conventional criterion. For a spectrum with multiple waves, β^j_{non} takes the form [*Medvedev and Klaassen*, 1995, 2000]

$$\beta^j_{non} = \frac{\sqrt{2\pi}N}{\sigma_j}\exp\left(-\frac{|c_j - \overline{u}|^2}{2\sigma_j^2}\right), \quad (3)$$

where the variance σ_j^2 is produced by velocity fluctuations due to harmonics with smaller than c_j intrinsic phase velocities $\sum_{mi>mj}\overline{u_i'^2}$, m being the vertical wave number.

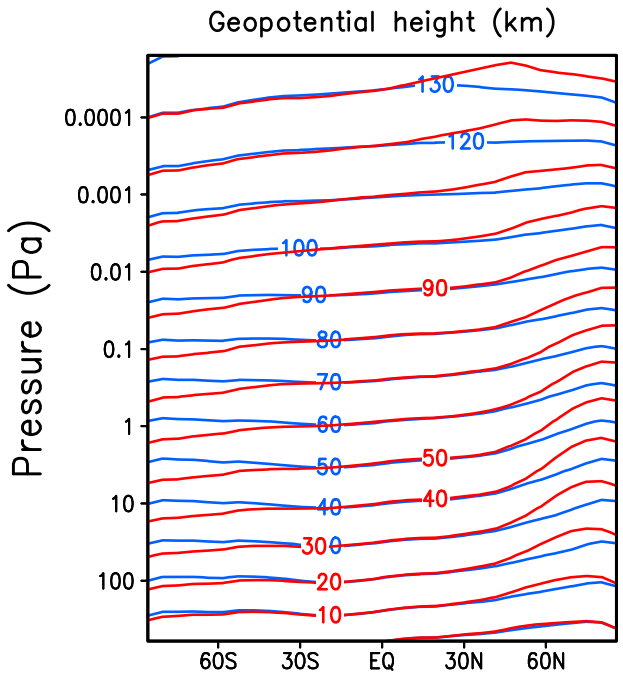

Figure 1. Zonal-mean geopotential heights (in km) simulated for L_s = 180° (blue lines) and L_s = 270° (red lines).

Other dissipative mechanisms that affect the vertical propagation of GWs (such as radiative damping, ion friction, eddy diffusion, etc.) can be accounted for by the scheme through an addition of the corresponding damping rates β in equation (1) [*Yiğit et al.*, 2008].

[11] If the wave flux F is known at the source level z_0, (1) can be integrated upward for all harmonics. The total momentum flux F is the sum of all components, and the net acceleration/deceleration ("GW drag") imposed by the spectrum is given by the divergence of F divided by the mean density (taken with the opposite sign):

$$a = -\rho^{-1}(\rho F)_z = -\sum_j \rho^{-1}(\rho F_j)_z \equiv \sum_j a_j, \qquad (4)$$

where a_j is the contribution from an individual harmonic.

[12] Kinematic molecular viscosity ν_{mol} is related to the coefficient of thermal conduction $k = AT^{0.69}$ via $k = 0.25[9c_p - 5(c_p - R)]\nu_{mol}$, where T is temperature, c_p and R are the specific heat at constant pressure and gas constant, respectively. For the pure CO_2 atmosphere under Martian conditions this yields $\nu_{mol} = 3.128T^{0.69} \times 10^{-7}/\rho$ [m^2 s^{-1}] [*Banks and Kockarts*, 1973]. These distributions adopted in our calculations are in a good agreement with the profile presented by *Parish et al.* [2009, Figure 2] and those used in the work of *González-Galindo et al.* [2009a]. The same kinematic viscosity has been applied to both the large-scale resolved motions and to the parameterized subgrid-scale GWs.

3. GCM Description

[13] The version of the Martian GCM employed in this study is the result of incremental upgrades of the model described in detail by *Hartogh et al.* [2005] and *Medvedev and Hartogh* [2007]. The major difference with the published versions is the use of a spectral dynamical core instead of a grid point (finite-difference) one.

[14] The model takes into account the radiative transfer in the gaseous CO_2, and the absorption, emission, and scattering by atmospheric dust. In the lower atmosphere, a local thermodynamic equilibrium (LTE) radiation scheme of *Nakajima et al.* [2000] based on the *k*-distribution method is used for the CO_2 15 μm band. Above, we employ an optimized version of the exact non-LTE code of *Kutepov et al.* [1998] and *Gusev and Kutepov* [2003]. This code relies on the accelerated lambda iteration solution, can be used with variable input of volume mixing ratios, and accounts for collisional quenching of CO_2 molecules by atomic oxygen, which are known to enhance CO_2 cooling in NLTE regions of the Martian upper atmosphere above ~100 km [*Bougher et al.*, 2009; *McDunn et al.*, 2010]. The heating/cooling rates computed by the LTE and non-LTE schemes are smoothly merged between 60 and 70 km, where both algorithms give virtually identical values. The radiative transfer in the dusty atmosphere is calculated using the scheme of *Nakajima and Tanaka* [1986] at 19 representative wavelengths: nine in the visible and ten in the infrared. The GCM accounts for thermal and mass effects of the CO_2 condensation and sublimation on the surface and in the atmosphere.

[15] The new dynamical core has been adopted from the Kühlungsborn Mechanistic General Circulation Model (KMCM), including the diffusion scheme as developed by *Becker* [2003] and *Becker and Burkhardt* [2007]. In the present study the spectral dynamical core is used with a triangular truncation at total horizontal wave number 21 which corresponds to ~1000 km for the shortest resolved horizontal wavelength. The vertical domain is discretized by 63 hybrid levels: terrain-following in the lower atmosphere, and pressure-based in the upper atmosphere. The model top has been placed at 1.6×10^{-5} Pa, that is, approximately at the Martian homopause. Figure 1 illustrates the geometrical vertical coverage of the model by presenting the geopotential heights calculated for the equinoctial (L_s = 180°) and solstitial (270°) seasons. As the thermospheric heating due to the absorption of solar radiation in UV and EUV was not taken into account in the current version of the GCM, the global-mean temperature gradient reversal in the lower thermosphere could not be reproduced in our simulations [*Bougher et al.*, 2006]. The model diffusion employs the Smagorinsky scheme with constant horizontal and vertical mixing lengths of 20 km and 30 m, respectively. In addition, horizontal wave numbers larger than 15 are subject to a weak hyperdiffusion, and the vertical diffusion includes the molecular diffusion plus a background vertical diffusion coefficient of 1 m^2 s^{-1}.

4. Observational Constraints on Gravity Waves and the Model Setup

[16] The GW parameterization requires a spectral distribution of wave momentum fluxes at a certain height chosen as a source level. These fluxes have not been measured on Mars, and experimental data on their detailed spatial and spectral compositions will likely not be available in the nearest future. Meanwhile, *Creasey et al.* [2006a] derived global and seasonal distributions of the GW activity in the

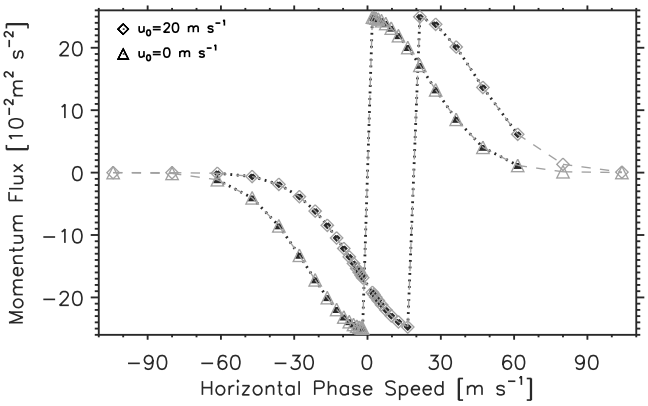

Figure 2. Momentum flux spectra (in $m^2\ s^{-2}$) at the source level (5) used in the simulations. Bold diamonds and triangles denote the fluxes for individual harmonics for two typical source level winds: u_0 = 20 and 0 m s^{-1}.

lower atmosphere from the Mars Global Surveyor (MGS) radio occultation data. They found that wave potential energy per unit mass, E_p, averaged between 10 and 30 km is typically up to several J kg^{-1} at middle- to high-latitudes. In low latitudes (~ ±20°) it increases up to 25 J kg^{-1}. For GWs with vertical wavelengths shorter than approximately one scale height, those which are considered by the scheme, *Creasey et al.* [2006a] find that E_p is about half as strong. The wave kinetic energy per unit mass, $E_k = \overline{u'2}/2$, is approximately equal to E_p for middle- and high-frequency GW harmonics [e.g., *Geller and Gong* 2010, equations 7–8]. This gives the estimate for the RMS variations of horizontal wave velocity: $|u'| = \sqrt{2E_p}$, or 1.4 to 4 m s^{-1}. Since the GW parameterization calculates the squared wave amplitudes $\overline{u_j'2}$ and the total horizontal wind variance $\overline{u'2} = \sum_j \overline{u_j'2}$ as byproducts, they can be used for adjusting the magnitudes of GW fluxes at the source level.

[17] High-altitude constraint on GWs follows from *Fritts et al.* [2006] who analyzed the Mars Odyssey aerobraking data in the Northern Hemisphere (NH) winter. They found that typical GW velocity perturbations $|u'|$ are ≈70 m s^{-1} at ~100 km or somewhat higher, and the associated GW momentum fluxes $\overline{u'w'} \approx 2000\ m^2\ s^{-2}$.

[18] The shape of the GW spectrum is another aspect of uncertainty. From a general perspective, amplitudes of fast harmonics must rapidly decay in order to avoid a divergence of the total integral over the spectrum. This does not mean, of course, that there cannot be local maxima in the phase velocity spectra associated with weather phenomena or tides. In our simulations we adopt the analytical form of the spectrum:

$$\overline{u'w'}_j = \mathrm{sgn}(c_j - \overline{u}_0)\,\overline{u'w'}_{\max} \exp\left[-(c_j - \overline{u}_0)^2 / c_w^2\right], \qquad (5)$$

where $\overline{u}_0$ is the mean wind at the source level and c_w is the half-width at half-maximum. This spectrum has been observed in the upper troposphere of Earth [*Hertzog et al.*, 2008], and was broadly used in terrestrial GCMs [*Yiğit et al.*, 2009, and references therein]. In the numerical experiments to be presented in the next sections, the spectrum is discretized with 28 harmonics, as shown in Figure 2 for two values of $\overline{u}_0$ = 0 and 20 m s^{-1}. It follows that although we employ a geographically uniform $\overline{u'w'}_{\max}$ = 0.0025 $m^2\ s^{-2}$ and c_w = 35 m s^{-1} in the GCM, the wave source will nevertheless vary in time and space because of the modulation by the simulated local wind $\overline{u}_0$ in the lower atmosphere. The direction of propagation of GW harmonics coincides with that of local wind at z_0 for $c_j > 0$ (positive momentum fluxes), and is against it for $c_j < 0$ (negative $\overline{u'w'}_{\max}$). The rationale for this anisotropic spectrum setup has been discussed in detail by *Medvedev et al.* [1998].

[19] Horizontal scales of wave fluctuations have been estimated between several tens and several hundreds km in both the lower and upper atmospheres. This provides a constraint on the characteristic horizontal wave number k_h, which is the only tunable parameter in our scheme (besides the source spectrum). In most terrestrial applications, it usually varies between $2\pi/100$ and $2\pi/(300\ km)$. $k_h = 2\pi/(300\ km)$ is used in all simulations described in this paper. Note that in case of purely dynamically induced damping of GWs (breaking and/or saturation), k_h serves as a scaling factor for the resultant drag [e.g., *Medvedev and Klaassen*, 1995, equation 28]: GWs with longer horizontal wavelengths deposit less momentum. If molecular viscosity is accounted for, waves with longer horizontal scales are damped more rapidly with increasing altitude, as follows from equation (2).

5. Results of GCM Simulations

[20] We next compare two simulations: with and without the GW parameterization. Unlike in many other GCMs, no sponge layer has been applied near the top of the model domain. Therefore, our results in the upper atmosphere are not contaminated by the influence of this artificial forcing, whose only purpose is to maintain the numerical stability of the model. The GW source height was at ≈260 Pa (~8 km), similar to the work of *Medvedev et al.* [2011], just above the altitudes frequently affected by convection. Although the latter can effectively excite GWs by disturbing stably stratified levels above, harmonics cannot propagate within convective cells themselves. More sensitivity tests concerning the source setup are described in section 6. The simulations have been performed with seasonally varying insolation, and results are presented in form of Martian monthly averages near the equinox (L_s = 180° to 210°) and solstice (L_s = 270° to 300°). For simplicity, the dust optical depth τ = 0.2 in visible wavelengths has been kept constant and uniformly distributed.

5.1. Equinox

[21] Figure 3 shows zonally averaged zonal winds from the two runs. Without GWs, the model produces a strong easterly jet in the upper atmosphere with velocities increasing with height (Figure 3a). Such a strong retrograde wind is an indication of a lack of wave-mean flow interaction [*Hide*, 1969]. Similar patterns have been reproduced by Martian GCMs without broad-spectra GW parameterizations [*Forget et al.*, 1999; *Haberle et al.*, 1999; *Hartogh et al.*, 2005; *González-Galindo et al.*, 2009a]. The westerly jets in both hemispheres in the "no-GW" run are closed up due to the negative momentum provided by dissipating large-scale (resolved) eddies, mainly tides. Addition of parameterized GWs modifies the simulated pattern significantly (Figure 3b). It is seen that the deposited GW

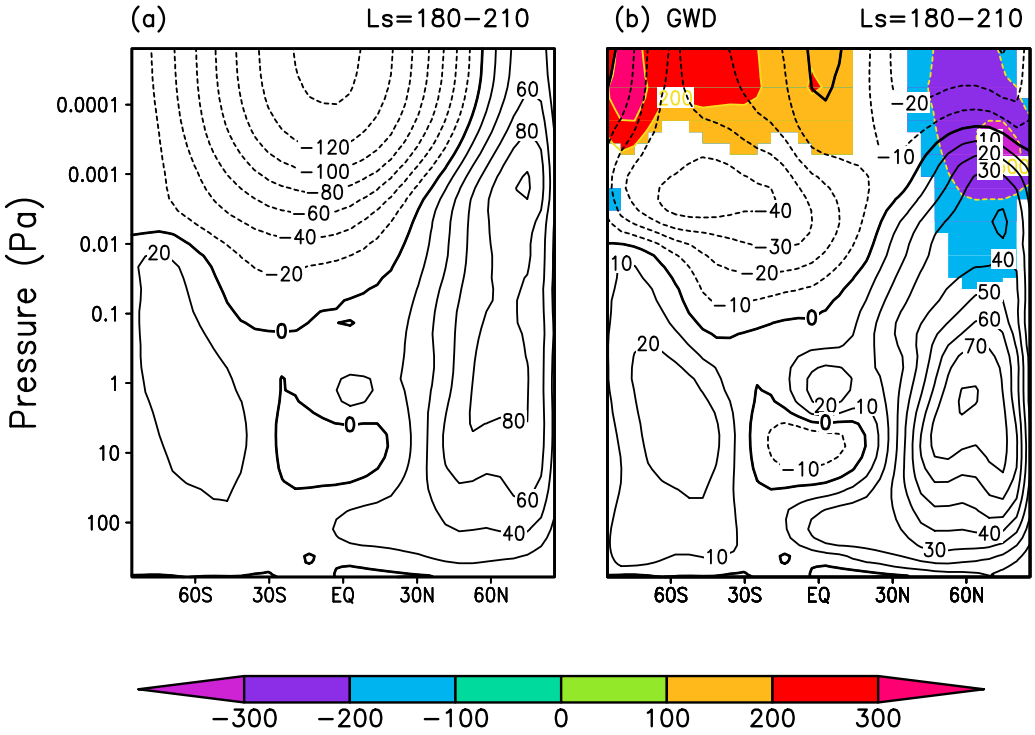

Figure 3. Mean zonal wind (contours, in m s^{-1}) and zonal drag (shaded, in m s^{-1} sol^{-1}) averaged between L_s = 180 and 210°: (a) The run without GWs. (b) The run with the GW scheme included.

momentum exceeds 300 m s^{-1} sol^{-1} and predominantly acts to decelerate the mean flow. This produces a lower reversal height of the westerly jet in the NH (~0.001 Pa or ~110 km), and significantly weaker easterlies. The shown GW drag represents both zonally and monthly averaged values, whereas instantaneously it can reach several thousands of m s^{-1} sol^{-1} above 100 km, well in accordance with measurement estimates [*Fritts et al.*, 2006; *Heavens et al.*, 2010]. The positive part of the GW drag is so strong that it tends to reverse the easterlies near the top of the model by the usual causality of the wave-driven residual circulation (text of *Andrews et al.* [1987]), that is, it drives an equatorward circulation that induces temperature changes and, in turn, a westerly adjustment of the zonal wind. A noticeable change is also seen in the equatorial atmosphere between 10 and 0.1 Pa (~30 and 80 km), where the signature of the semiannual oscillation is enhanced by GWs. This effect is well known from the terrestrial middle atmosphere [*Medvedev and Klaassen*, 2001].

[22] The zonally averaged meridional wind and the corresponding meridional GW drag are plotted in Figure 4. Two hemispheric meridional cells extend from the surface into the upper atmosphere in the run without GWs. A slight asymmetry occurs because the averaging period is shifted with respect to the orbital equinox. The two cells merge into a pole-to-pole upper branch of the meridional circulation when GWs are included. Although the meridional GW drag is about three times weaker than the zonal one, it is quite strong to significantly alter the gradient wind balance. Therefore, the meridional GW drag will directly drive changes of the mean zonal wind. The positive meridional GW drag in the Southern Hemisphere (SH) and the negative in the NH act against the wind reversal induced by the zonal drag. The meridional wind changes from 80 to 40 m s^{-1} in the NH, and from −35 to −20 and even to +20 m s^{-1} in the SH. While the change in the SH can be attributed to the positive zonal GW drag (Figure 3), the reduction of the poleward flow in the NH cannot be attributed to the negative zonal GW drag. It is rather related to GW-induced changes of the resolved waves (mainly tides), which exert a strongly negative zonal drag in the run without GWs and a weaker one when GWs are included (not shown). The magnitudes of the zonal mean meridional GW drag vary between −110 and 80 m s^{-1} sol^{-1}, although instantaneously it is comparable to the zonal drag values of thousands of m s^{-1} sol^{-1}. A closer look also shows that below p = 0.01 Pa (or 90–100 km), the poleward flow increases by few m s^{-1} in the NH when GWs are included.

[23] Changes of the wind driven by changes of the drag due to parameterized GWs and resolved waves give rise to a response in the thermal structure via the adiabatic heating/cooling rates associated with the altered circulation. The two simulated temperature fields are plotted in Figure 5 with contours, and their differences with color shades. Compared to the dataset of temperature retrievals from Mars Climate Sounder onboard the Mars Reconnaissance Orbiter (MRO–MCS) for MY29 [*McCleese et al.*, 2008, 2010], the model without GWs reproduces well the temperature in the lower atmosphere, overestimates it by 5–10 K in tropics between 1 and 0.1 Pa, and underestimates the polar temperature by 10 K over the South Pole and by 20 K over the North at ~1 Pa. Overall, it indicates that the simulated two-cell circulation is somewhat weaker than follows from the temperature retrievals. However, given our simplified uniform

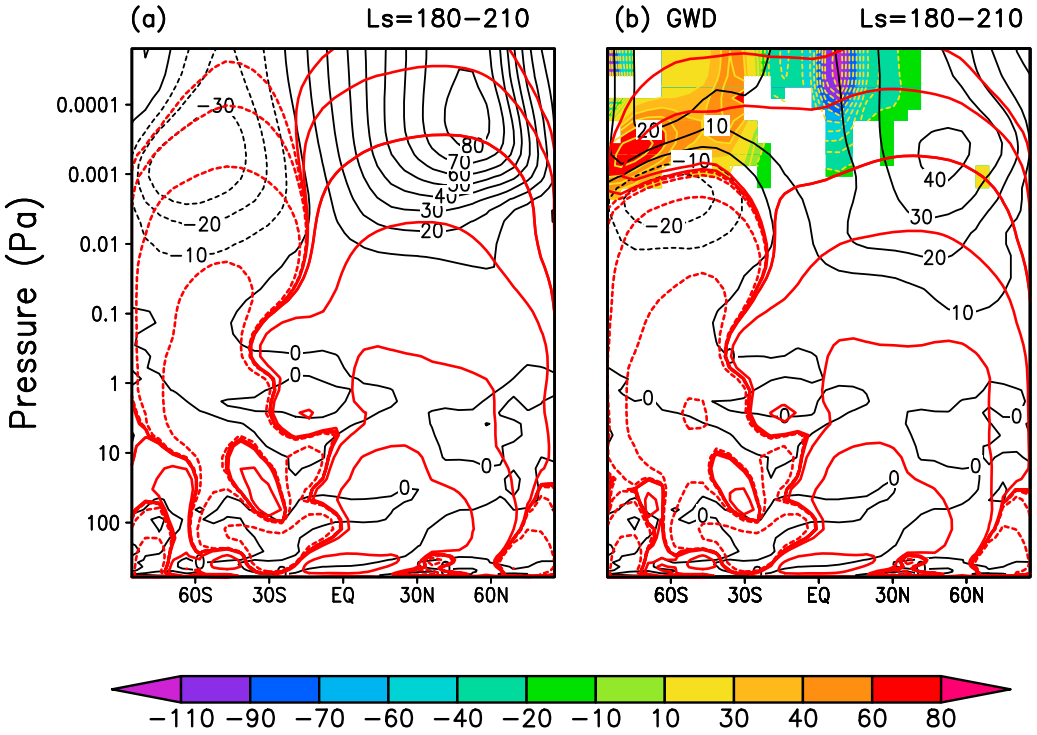

Figure 4. Same is in Figure 3 but for the meridional components of the wind and GW momentum deposition. Superimposed are the Eulerian mean meridional stream functions.

dust distribution as well as the fact that MRO–MCS dataset is represented by only one nighttime, and one or two daytime measurements, the agreement between the model and data is reasonably good. The major temperature alteration caused by GWs occurred in the upper portion of the domain where the GW drag is the strongest, as well as in both polar regions between p = 1 and 0.01 Pa. Adiabatic heating due to the intensification of the poleward circulation cells

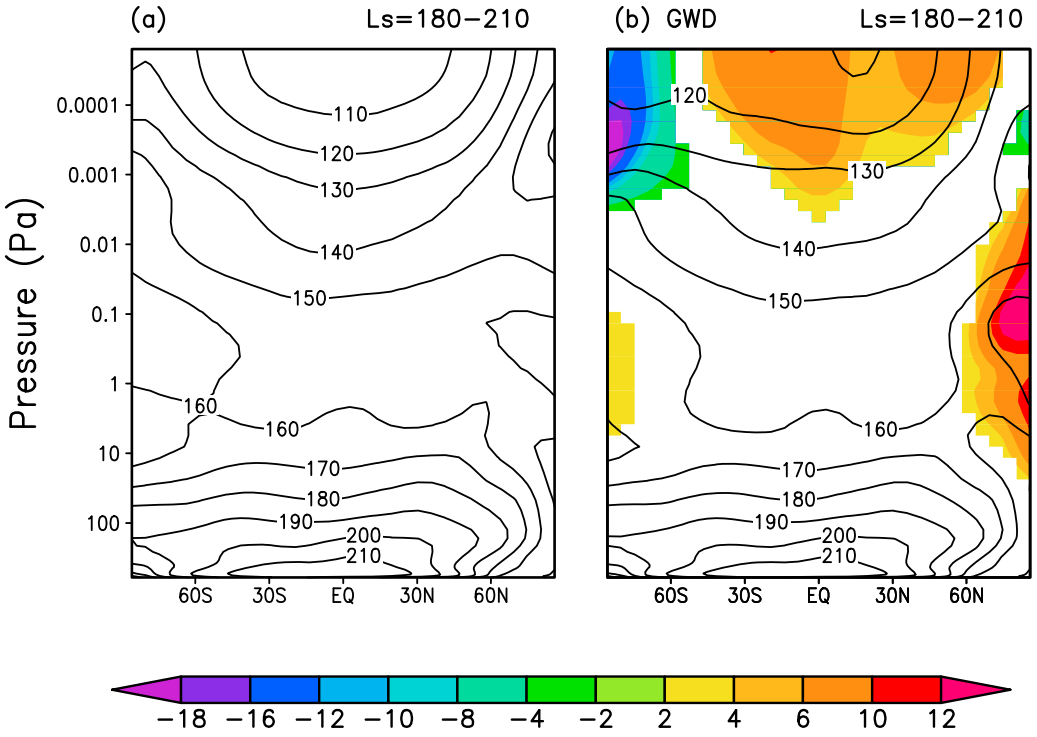

Figure 5. Same as in Figure 3 but for the temperature (contour lines, in K). The differences between the run with and without parameterized GWs are shown in color shades.

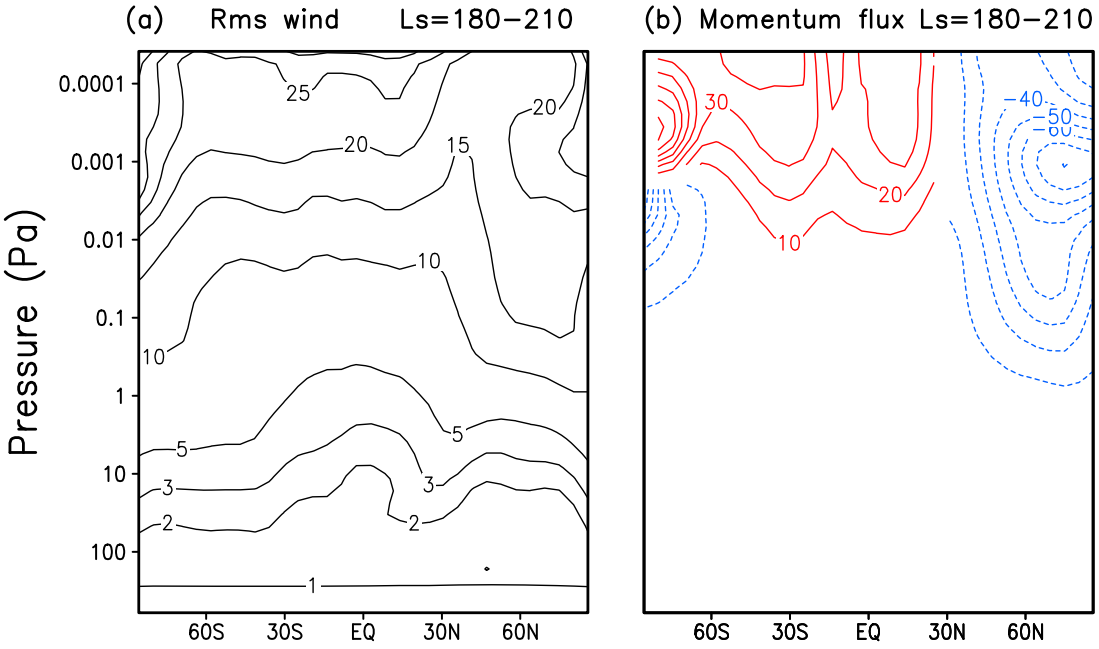

Figure 6. (a) RMS horizontal wind fluctuations (m s^{-1}) associated with GWs and (b) horizontal wave momentum fluxes (m^2 s^{-2}) averaged zonally and between L_s = 180 and 210°.

produces more than 12 K warmer temperatures in the NH, and +2 to 3 K in the SH. Above 0.01 Pa, the opposite takes place: the atmosphere is more than 18 K colder over the South Pole, and few degrees colder in the Northern high latitudes. In the low- and middle latitudes, the temperature is up to 10 K warmer in the run with GWs. It is worth emphasizing again that the direct thermal effects of dissipating GW harmonics as studied by *Yiğit and Medvedev* [2009] were not taken into account in our simulations, and these changes in temperature are driven exclusively by the changes of the parameterized and resolved wave drag.

[24] The calculated characteristics of the parameterized GW field are presented in Figure 6 in the form of zonally averaged RMS horizontal wind fluctuations, $|u'| = (\overline{u'^2})^{1/2}$, and the vertical flux of horizontal momentum, $\overline{u'w'}$. At the source height, $|u'|$ is ≈1 m s^{-1}, that is, at the lower end of the *Creasey et al.* [2006a] estimates. Above 100 km, the RMS wind amplitude is up to 25 m s^{-1} in the zonal mean, and can reach up to 50 m s^{-1} instantaneously. This is smaller than the values up to 70 m s^{-1} given by *Fritts et al.* [2006]. The distribution of GW momentum fluxes in Figure 6b reflects the selective transmission of harmonics by the mean wind. Since waves traveling against the wind are less affected by damping and filtering, westward momentum fluxes dominate the upper atmosphere in the Northern mid- and high latitudes, and eastward fluxes associated with fast harmonics prevail in the SH. The averaged magnitudes of their fluxes are relatively small (tens m^2 s^{-2}) compared to observations [*Fritts et al.*, 2006], but instantaneous values are up to 300 m^2 s^{-2}.

5.2. Solstice

[25] More dramatic changes take place when the parameterized GWs are included in the simulations during solstices. Both prograde and retrograde jets extend to the top of the model when the GW drag is not accounted for (Figure 7a), where only the dissipation of tides and other resolved large-scale eddies by molecular diffusion and thermal conduction prevents them from growing with height further. If the molecular viscosity is set to zero, both jets have a tendency to accelerate and eventually to make the model unstable. If GWs are included, the simulated jets close up between 100 and 130 km (Figure 7b). This pattern is very similar to the one in the terrestrial MLT between 80 and 110 km. The instantaneous GW torque can reach thousands of m s^{-1} sol^{-1}, which is in a good agreement with observations [*Fritts et al.*, 2006; *Heavens et al.*, 2010] and modeling estimates [*Barnes*, 1990; *Joshi et al.*, 1995; *Collins et al.*, 1997]. Its zonally and temporally averaged values are hundreds of m s^{-1} sol^{-1} of both signs (shaded in Figure 7b) with the easterly drag in the winter hemisphere being almost twice stronger than the westerly drag in the summer. Such distributions are fully consistent with the selective filtering of GW harmonics by the zonal wind below, which is accompanied by an acceleration of the underlying jets. This acceleration is weak (few m s^{-1} sol^{-1}) and not seen in the figure due to the chosen contour intervals.

[26] The solstitial meridional circulation in the upper atmosphere of Mars is dominated by the strong summer-to-winter hemisphere transport cell. In the absence of a parameterized forcing by subgrid-scale GWs (Figure 8a), it is driven by the momentum transported upwards by dissipating large-scale planetary waves and tides. The main effect of GWs, as in equinoxes, is to decelerate the mean meridional wind (Figure 8b) by the combined changes of the resolved and parameterized zonal drag. The meridional flow intensifies to 90 m s^{-1} around 50°N as a result of the strong westward GW drag in this region. This, in turn, causes stronger downwelling over the pole and the corresponding winter polar warming (see Figure 9b). The magnitudes of

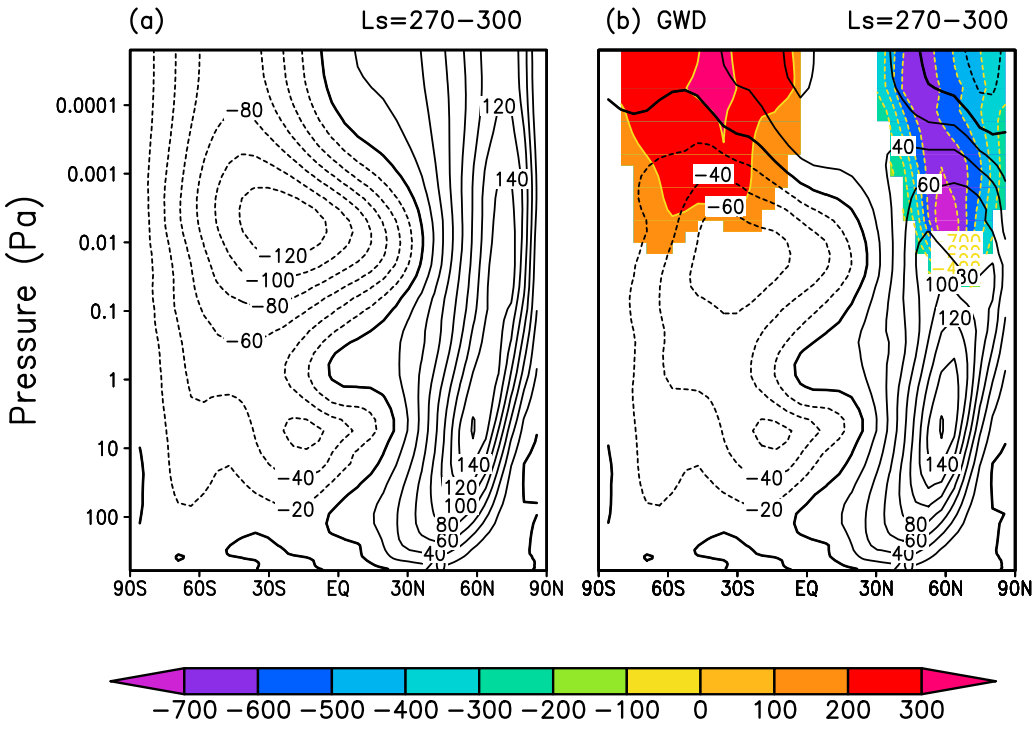

Figure 7. Mean zonal wind (contours, in m s^{-1}) and zonal drag (shaded, in m s^{-1} sol^{-1}) averaged between L_s = 270 and 300°: (a) The run without GWs. (b) The run with the GW scheme included.

the zonally averaged meridional drag are much stronger (hundreds of m s^{-1} sol^{-1}) during the solstices than during equinoxes. A gap in the meridional drag is clearly seen in Northern Hemisphere midlatitudes. In our simulations, it can be traced to the strong polar night jet in the lower atmosphere, where the GWs are launched. The direction of the wind at the source level is mainly eastward, and meanderings of the jet due to the enhanced baroclinic activity

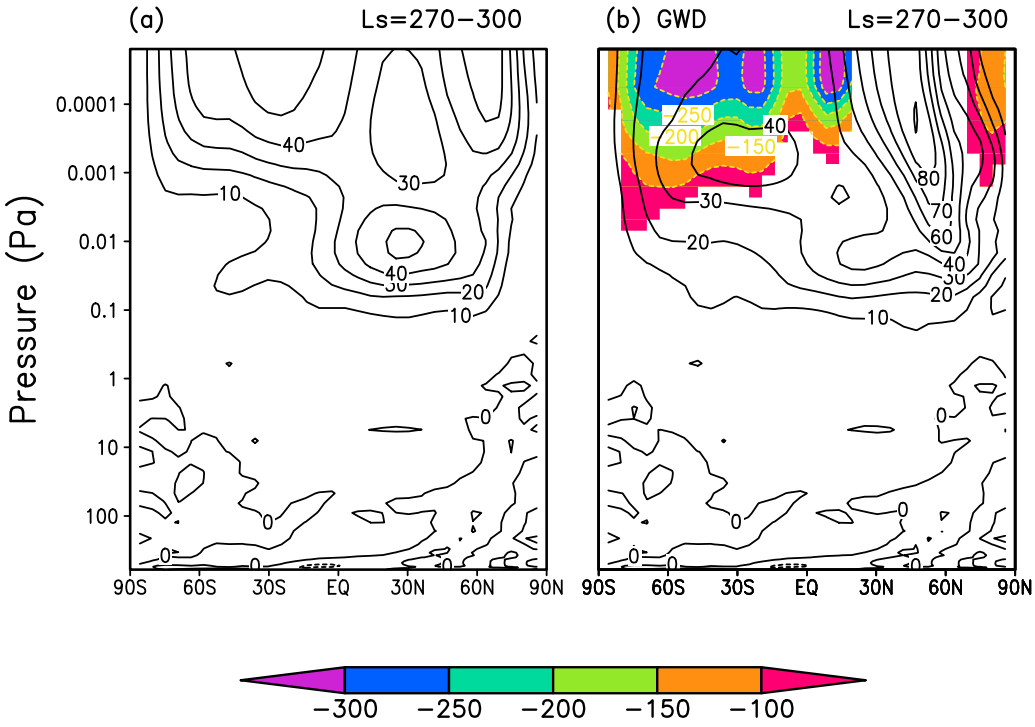

Figure 8. Same is in Figure 7 but for the meridional components of the wind and GW momentum deposition (in m s^{-1} sol^{-1}).

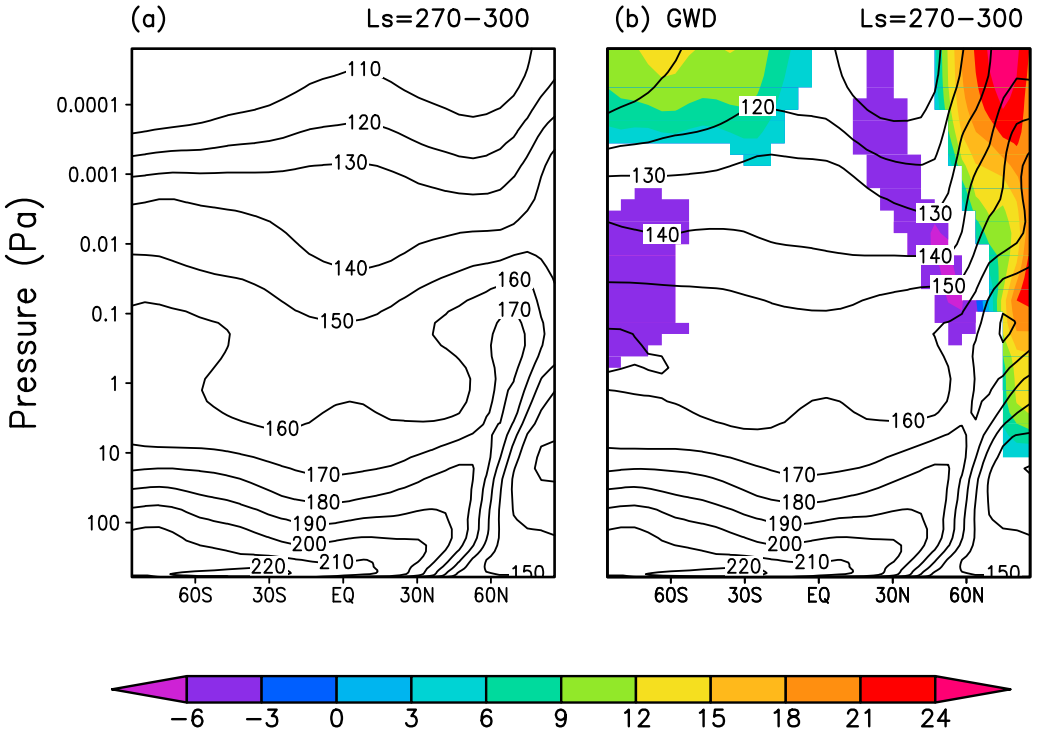

Figure 9. Same as in Figure 7 but for the temperature (contour lines). The differences between the run with and without parameterized GWs are shown in color shades.

[*Kuroda et al.*, 2007] largely cancel out the meridional components of the wind when temporally and spatially averaged. Therefore, the amount of waves having the meridional component, and the corresponding GW momentum deposition sharply decreases. In essence, our simulations point out to a possibly important role of GWs in the vertical coupling of the lower and upper atmospheres of Mars. In particular and differently from the transformed Eulerian mean equations usually applied for diagnostics of the terrestrial atmosphere, gradient wind balance must by complemented by the strong meridional GW drag.

[27] Changes in the temperature are closely related to alterations/decelerations of the meridional circulation due to parameterized GWs. Without GWs, the simulated temperature below 0.1 Pa agrees well with the MRO–MCS dataset for MY29 [*McCleese et al.*, 2010] almost everywhere except over the North Pole above 1 Pa, where the simulated temperature is 30 to 40 K colder. With GWs, the mean temperature increases over the winter pole having two maxima of more than 24 K: at 0.1 Pa (~75 km) and 10^{-4} Pa (~130 km), exactly where the Martian middle atmospheric [*Medvedev and Hartogh*, 2007; *McCleese et al.*, 2008] and thermospheric warmings occur [*Bougher et al.*, 2006; *McDunn et al.*, 2011]. The magnitudes of the warmings are also in line with the modeling for the low dust season (180 K at p = 0.1 Pa) [*Medvedev and Hartogh*, 2007]) and observations (150–160 K at p = 10^{-3} Pa) [*Bougher et al.*, 2006]). Obviously, the exact shape and values of the temperature field depend on GW sources in the lower atmosphere, and it might be too speculative to assume that GW activity near the polar cap during winter nights is the same as in other parts of the globe. A caution should also be exercised as our simulations did not include UV and EUV heating. Although such warmings are locally adiabatic, they are sensitive to the radiative forcing in the thermosphere at sunlit latitudes [*Bougher et al.*, 2009; *González-Galindo et al.*, 2009b]. However, our simulations clearly demonstrate that both winter polar temperature maxima are related and significantly influenced by small-scale GWs. The other noticeable changes in the simulated fields include up to 14 K higher temperatures in the summer hemisphere above 10^{-3} Pa (~115 km), and ~5 K colder midlatitudes of the winter hemisphere and South Pole region below 110 km. It seems plausible that some of these GW-induced changes can explain anomalously colder temperatures observed by Mars Express SPICAM at these altitudes [*Forget et al.*, 2009].

[28] Averaged RMS wind fluctuations associated with GWs and the wave momentum fluxes (Figure 10) demonstrate a rapid filtering of eastward propagating harmonics by the westerly polar night jet in the NH. Instantaneous values of $|u'|$ (not shown) are up to 60 m s^{-1} near the top of the model domain, which is in line with 70 m s^{-1} obtained by *Fritts et al.* [2006]. The instantaneous values of the momentum flux $\overline{u'w'}$ are up to ±600 m^2 s^{-2}, which is less than the 2000 m^2 s^{-2} estimate of *Fritts et al.* [2006]. Since the momentum flux is a vector quantity, the total flux is not entirely suitable for characterizing GW fields consisting of multiple harmonics. For instance, two waves with large amplitudes (and, therefore, having large fluxes) but traveling in opposite horizontal directions (with opposite signs of momentum fluxes) can produce small or even zero net momentum flux. The RMS wind fluctuation amplitude,

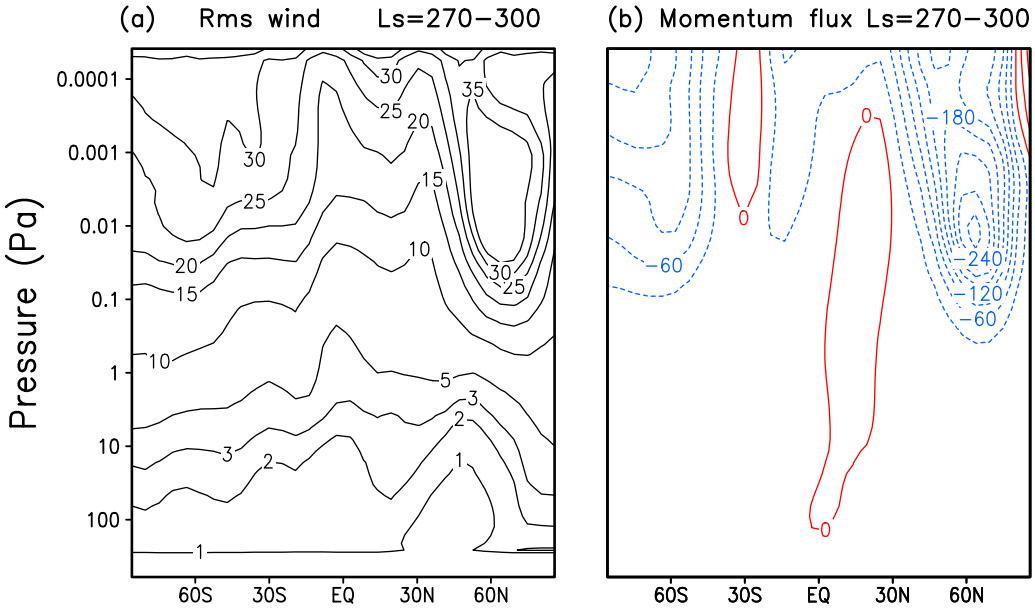

Figure 10. (a) RMS horizontal wind fluctuations associated with GWs (m s^{-1}) and (b) horizontal wave momentum fluxes (in m^2 s^{-2}) averaged zonally and between L_s = 270 and 300°.

a positively defined quantity, is more useful for comparing simulations and observations.

6. Sensitivity to the Wave Sources

[29] The results of the previous section demonstrated a strong dynamical influence of small-scale GWs propagating from below on the upper atmosphere of Mars. Given the uncertainties in GW sources in the lower atmosphere, how robust are our results? To investigate this issue, a series of sensitivity tests has been performed under the conditions of a perpetual Northern winter solstice at L_s = 270°. As before, the dust optical depth in visible wavelengths τ = 0.2 was kept constant and uniform. In each experiment, the model has been spun up for 100 sols, and the output of the last 5 sols has been averaged. The results are summarized in Figure 11.

[30] Figures 11a to 11c present the zonal and meridional wind, and temperature, respectively, in the benchmark simulation with the same GW source as in the previous section. Comparing with Figures 7–9, one can conclude that the run with the fixed L_s = 270° captures all the features of the simulation with the seasonally varying insolation: the closure and reversals of the zonal jets, weakening of the meridional transport, values of the simulated fields, a gap in the zonal drag in the Northern Hemisphere midlatitudes, and the related changes in the upper atmospheric temperature. In fact, the two simulations resemble each other very closely.

[31] In the next simulation shown in Figures 11d, 11e, and 11f, the very same GW source is placed lower, only few hundred meters above the surface (at $\sigma = p/p_s = 0.89$, p_s being the surface pressure). Thus, GW harmonics have additional vertical distance to travel and grow in amplitude due to the density stratification. This is approximately equivalent to increasing the value of $\overline{u'w'}_{max}$ in (5) of the benchmark run. The simulated fields confirm this view accordingly: the magnitudes of both the zonal and meridional drag are larger, and breaking/saturation of GWs takes place lower. As a result, the westerly jet in the winter hemisphere is ~20 m s^{-1} weaker (130 vs 150 m s^{-1}), and the reversal occurs lower. A noticeable difference is in the distribution of the meridional wind and drag. The gap in the GW momentum deposition in midlatitudes of the NH is now filled, and the mean meridional wind in the mesosphere is up to 20 m s^{-1} weaker. Further diagnostics reveals that this occurred because of a stronger jet meandering near the surface associated with baroclinic wave activity. As the GW harmonics were launched in the direction of the local wind, more meridional momentum flux was injected at the source level, and, ultimately, more meridional drag was deposited in the upper atmosphere.

[32] The magnitude of the source, $\overline{u'w'}_{max}$, has been increased ten-fold to 0.025 m^2 s^{-2} in the simulation presented by Figures 11g, 11h, and 11i. The GW launch height was kept the same as in the benchmark run. The simulated zonal wind is weaker because the amplitudes of the waves are larger, and, accordingly, their saturation occurs lower. These waves were either filtered out at lower heights or significantly damped during their upward propagation, therefore the magnitude of the jet reversal they produce is smaller. For instance, the westerlies in the summer hemisphere near the top of the model are ~10 m s^{-1} weaker than in Figure 11a. The lack of the meridional drag and the corresponding strong poleward flow are seen in midlatitudes of the winter hemisphere (Figure 11h). It is the result of the relative deficit of GW meridional momentum at the source level despite its ten-fold magnification. The simulated winter polar warming in the middle atmosphere is ~19 km lower than in the benchmark run, but the corresponding upper atmospheric temperature is marginally warmer, and, generally, even colder than in Figure 11c. Overall, it is seen that increasing the magnitude of GW sources and placing

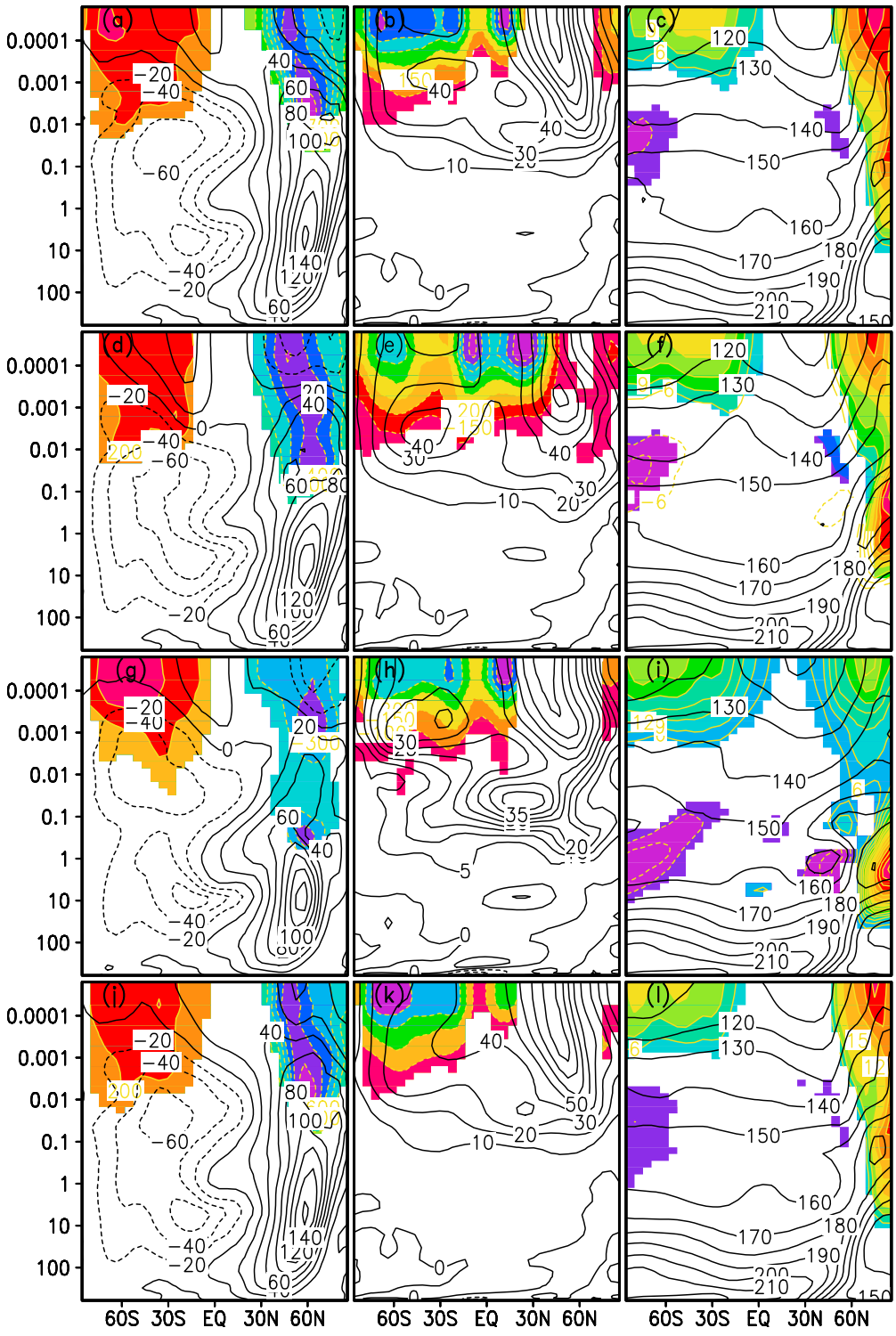

Figure 11. Sensitivity tests for a perpetual Northern winter (L_s = 270°). (a, d, g, j) The simulated zonal winds (contours, in m s^2) and GW drag (shaded, in m s^{-1} sol^{-1}). (b, e, h, k) The meridional winds (contours) and the meridional GW drag (shaded). (c, f, i, l) The mean zonal temperatures (contours) and the deviations from the run without GW scheme (shaded). The benchmark run is shown in Figures 11a, 11b, and 11c. The run with the GW source placed near the surface is shown in Figures 11d, 11e, and 11f. The run with 10-fold increased GW source amplitude is shown in Figures 11g, 11h, and 11i. The run with the additional radiative damping of GWs included is shown in Figures 11j, 11k, and 11l.

them lower produce although not identical, but in many ways similar changes in simulated fields.

7. Impact of Radiative Damping on Gravity Waves

[33] Recently, *Eckermann et al.* [2011] quantified the IR radiative damping of small-scale GWs on Mars to demonstrate that it is much stronger than on Earth due to almost 95% CO_2 atmosphere. They suggested that this mechanism of wave attenuation in the Martian atmosphere competes with, and even dominates the molecular viscosity and nonlinear breaking/saturation. Our next sensitivity experiment (Figures 11j, 11k, and 11l) has been designed to test the influence of the radiative damping on GW momentum flux deposition and the corresponding dynamical feedback of the circulation. The IR damping rates, $\alpha = \tau_d^{-1}$, where τ_d is the characteristic damping time *Eckermann et al.* [2011], are strong functions of height and the vertical wavelength. Besides that, they depend on vertical profiles of temperature. *Eckermann et al.* [2011] have calculated τ_d^{-1} only for a certain temperature distribution. Therefore, in our implementation, we approximated α by a single function of altitude, similar to the profile of τ_d^{-1} for the harmonic with the vertical wavelength 5 km [*Eckermann et al.*, 2011, Figure 5]. It monotonically grows with height, reaches the maximum of 25 $sols^{-1}$ at ≈120 km, and then decays to 18 $sols^{-1}$ near the model's top. The corresponding vertical damping rate for the GW flux has the form [*Yiğit et al.*, 2008, section 3.5]:

$$\beta_{rad}^{j} = \frac{2\alpha N}{k_h \left| c_j - \overline{u} \right|^2}. \tag{6}$$

It is seen from (6) that vertical damping rates are still scale selective despite α not being a function of wavelength: harmonics with shorter vertical wavelength are attenuated more. In the simulation, (6) has been added to other damping rates in (1), and the run performed with the benchmark GW source.

[34] Surprisingly as it may be seen at a first glance, the simulated fields (Figures 11j, 11k, and 11l) are very close to those without β_{rad} taken into account (Figures 11a, 11b, and 11c). More detailed analysis shows that the radiative damping indeed dominates the molecular viscosity and breaking/saturation of the parameterized harmonics in the lower atmosphere. Since the amplitudes of GWs are small there, the drag associated with the additional dissipation of momentum fluxes is small too. When wave amplitudes attain the breaking/saturation threshold, the increase of β_{non} is very rapid, and the nonlinear damping generally exceeds the radiative one above ~80 km. Yet higher, the molecular viscosity competes with β_{non}, and eventually dominates all other dissipation mechanisms as ν_{mol} is inversely proportional to exponentially decaying atmospheric density. Since mostly fast harmonics with large vertical wavelengths survive in the upper atmosphere, IR radiative damping affects them less, and its contribution to the wave flux attenuation is not so strong compared to that by molecular viscosity. Radiative damping increases when a refraction by the mean wind shifts harmonics to smaller vertical wavelengths. However, this usually occurs just below breaking/saturation levels, and the overall effect of additional (β_{non}) dissipation on the GW drag tends to be small.

8. Summary and Conclusions

[35] The implementation of our recently developed extended spectral nonlinear gravity wave (GW) parameterization [*Yiğit et al.*, 2008] into the Martian GCM extended to ~130 km have revealed a strong dynamical influence of the small-scale GWs of lower atmospheric origin on the circulation between 100 and 130 km. Interactive simulations confirm our conclusion based on estimates with the Mars Climate Database output wind [*Medvedev et al.*, 2011] that GWs give rise to deceleration of the zonal winds at all seasons, and even produce reversals in the upper part of the Martian mesosphere (100–130 km) at solstices, similar to those in the terrestrial MLT (70–110 km). These reversals are driven by the momentum deposited by dissipating/breaking/saturating GW harmonics with non-zero observed phase speeds. Such waves have not been accounted for in the previous studies of the Martian atmosphere, and, therefore, neither the zonal jet reversals nor the dominant role of GWs in the upper atmosphere dynamics of Mars have been revealed.

[36] The net effect of the parameterized GWs on the mean zonal wind is to decelerate and even reverse it increasingly with height. Zonal mean values of the GW torque are hundreds of m s^{-1} sol^{-1}, instantaneously it can be as large as thousands of m s^{-1} sol^{-1}, well in accordance with observational and theoretical estimates. Besides the strong influence on the mean zonal wind, our simulations show that GWs give rise to strong changes of the meridional wind, which even transforms a two-cell meridional equinoctial circulation into a pole-to-pole transport. Instantaneous values of the meridional drag are similar to those of the drag in the zonal direction (thousands of m s^{-1} sol^{-1}), although in the mean they are somewhat smaller than the zonal ones. Temperature changes associated with the dynamical effects of GWs are significant above ~100 km, but complex. The most obvious is the enhancement of both the "middle atmosphere" (~70 km) and "upper atmosphere" (~130 km) winter polar warmings. The changes in the other parts of the upper atmosphere and at different seasons are related to the alterations of the circulation, and range from −15 to 15 K on average.

[37] Although our GW scheme has virtually no "tuning parameters", it still requires a spectral distribution of horizontal momentum fluxes at a certain vertical level in the lower atmosphere taken as a source height. The exact temporal, geographical, and spectral distributions of GWs are far beyond our knowledge not only on Mars, but on Earth as well. Even the most advanced comprehensive terrestrial GCMs often approximate them by spatially uniform, constant in time model functions composed of averaging of many observations. The same approach was used in this study, and a simplified GW source was employed, which produced the "best" results with GCMs on Earth. The constraints at the lower boundary were provided by the MGS radio occultation data [*Creasey et al.*, 2006a]. The simulated GW RMS wind fluctuations and momentum fluxes in the upper atmosphere were compared to the observations of *Fritts et al.* [2006] and *Creasey et al.* [2006b]. The calculations have been performed

with the modest source magnitude taken at the lower end of the constraining range of GW RMS velocities. The simulated wave amplitudes and fluxes turned out to be in a good agreement with observations.

[38] Given the uncertainties of GW sources and despite the agreement of the simulated and observed wave parameters, we performed sensitivity experiments to test the robustness of our results. Several of them we presented in the paper. Increasing the amplitude of the source, placing it on the ground (instead of ~8 km), accounting for the additional CO_2 radiative damping, as was suggested by *Eckermann et al.* [2011], did not alter the simulated patterns and values significantly and, thus, did not change the main conclusion regarding the dynamical importance of GWs. Even less modifications were produced by broadening the source spectrum with c_w or extending its range to include faster harmonics. These harmonics tend to penetrate higher into the upper atmosphere since they 1) require larger amplitudes to reach saturation/breaking threshold, and 2) are less affected by molecular viscosity. In our calculations, they propagate through the vertical model domain without depositing a noticeable momentum and producing changes in the circulation. Overall, our study demonstrates that the effects of small-scale GWs at 100–130 km is strong and robust, and that these waves constitute an important part of the dynamics of the Martian mesosphere. The study also shows why the significance of GWs has not been found below 100 km.

[39] It is noteworthy that, although the large GW drag and its strong dynamical impact are broadly consistent with what has been derived from observations, our results still have predictive character. The best existing systematic measurements from Mars Climate Sounder aboard the Mars Reconnaissance Orbiter (MRO-MCS) extend to approximately 80 km, and there are no sufficient observations covering the upper mesosphere and lower thermosphere of Mars. Wind measurements can provide the most direct information for verifying our predictions, and for constraining GW parameterizations in the future. Some results have been obtained by *Baird et al.* [2007] who retrieved instantaneous values of the zonal wind from the accelerometer data during the aerobraking phase of Mars Global Surveyor. They were spread over the L_s = 215 to 300° season, and covered the altitudes between 115 and 135 km at midlatitudes of the Northern Hemisphere. Although the instantaneous values contained variations due to tides and planetary waves, the inferred westward wind is more consistent with our simulations with GWs [*Baird et al.*, 2007, Figure 9], especially for the solstice. The other source of data that can help to constrain the mesospheric effects of GWs in GCMs are measurements of the wave-related activity in the lower atmosphere.

[40] The predicted dynamical importance of GWs, if confirmed by future measurements, may substantially change our understanding of the circulation in the Martian upper atmosphere, and of the vertical coupling between atmospheric layers. It may also indicate a universal significance of GWs in planetary atmospheres. Improved description of the wind and density at these heights may affect aerobraking operations of spacecraft. The Mars Atmosphere and Volatile Evolution (MAVEN) mission scheduled for launch in 2013 can provide the required data for validation of our predictions.

[41] **Acknowledgments.** We thank Scot Rafkin and the anonymous referee for helpful comments. This work was partially supported by German Science Foundation (DFG) grant HA3261/4,5.

References

Andrews, D. G., J. R. Holton, and C. B. Leovy (1987), *Middle Atmosphere Dynamics*, 489 pp., Academic Press, San Diego, Calif.

Baird, D. T., R. Tolson, S. Bougher, and B. Steers (2007), Zonal wind calculations from Mars Global Surveyor accelerometer and rate data, *J. Spacecraft Rockets*, *44*, 1180–1187.

Banks, P. M., and G. Kockarts (1973), *Aeronomy Part B*, 355 pp., Elsevier, New York.

Barnes, J. R. (1990), Possible effects of breaking gravity waves on the circulation of the middle atmosphere of Mars, *J. Geophys. Res.*, *95*, 1401–1421.

Becker, E. (2003), Frictional heating in global climate models, *Mon. Weather Rev.*, *131*, 508–520.

Becker, E., and U. Burkhardt (2007), Nonlinear horizontal diffusion for GCMs, *Mon. Weather Rev.*, *135*, 1439–1454.

Bougher, S. W., S. Engel, D. P. Hinson, and J. R. Murphy (2004), MGS Radio Science electron density profiles: Interannual variability and implications for the neutral atmosphere, *J. Geophys. Res.*, *109*, E03010, doi:10.1029/2003JE002154.

Bougher, S. W., J. M. Bell, J. R. Murphy, M. A. Lopez-Valverde, and P. G. Withers (2006), Polar warming in the Mars thermosphere: Seasonal variations owing to changing insolation and dust distributions, *Geophys. Res. Lett.*, *33*, L02203, doi:10.1029/2005GL024059.

Bougher, S. W., P.-L. Bielly, M. Combi, J. L. Fox, I. Mueller-Wodarg, A. Ridley, and R. G. Roble (2008), Neutral upper atmosphere and ionosphere modeling, *Space Sci. Rev.*, *139*, 107–141, doi:10.1007/s11214-008-9401-9.

Bougher, S. W., T. M. McDunn, K. A. Zoldak, and J. M. Forbes (2009), Solar cycle variability of Mars dayside exospheric temperatures: Model evaluation of underlying thermal balances, *Geophys. Res. Lett.*, *36*, L05201, doi:10.1029/2008GL036376.

Bougher, S. W., A. Ridley, D. Pawlowski, J. M. Bell, and S. Nelli (2011), Development and validation of the ground-to-exosphere Mars GITM code: Solar cycle and seasonal variations of the upper atmosphere, paper presented at Fourth International Workshop on the Mars Atmosphere: Modelling and Observations, NASA, 8–11 February, Paris.

Creasey, J. E., J. M. Forbes, and D. P. Hinson (2006a), Global and seasonal distribution of gravity wave activity in Mars' lower atmosphere derived from MGS radio occultation data, *Geophys. Res. Lett.*, *33*, L01803, doi:10.1029/2005GL024037.

Creasey, J. E., J. M. Forbes, and G. M. Keating (2006b), Density variability at scales typical of gravity waves observed in Mars' thermosphere by the MGS accelerometer, *Geophys. Res. Lett.*, *33*, L22814, doi:10.1029/2006GL027583.

Collins, M., S. R. Lewis, and P. L. Read (1997), Gravity wave drag in a global circulation model of the Martian atmosphere: Parameterization and validation, *Adv. Space Res.*, *19*(8), 1245–1254.

Eckermann, S. D., J. Ma, and X. Zhu (2011), Scale-dependent infrared radiative damping rates on Mars and their role in the deposition of gravity-wave momentum flux, *Icarus*, *211*, 429–442.

Forget, F., F. Hourdin, R. Fournier, C. Hourdin, O. Talagrand, M. Collins, S. R. Lewis, P. L. Read, and J.-P. Huot (1999), Improved general circulation models of the Martian atmosphere from the surface to above 80 km, *J. Geophys. Res.*, *104*, 24,155–24,175.

Forget, F., F. Montmessin, J.-L. Bertaux, F. González-Galindo, S. Lebonnois, E. Quémerais, A. Reberac, E. Dimarellis, and M. A. López-Valverde (2009), Density and temperatures of the upper Martian atmosphere measured by stellar occultations with Mars Express SPICAM. *J. Geophys. Res.*, *114*, E01004, doi:10.1029/2008JE003086.

Fritts, D. C., L. Wang, and R. H. Tolson (2006), Mean and gravity wave structures and variability in the Mars upper atmosphere inferred from Mars Global Surveyor and Mars Odyssey aerobraking densities, *J. Geophys. Res.*, *111*, A12304, doi:10.1029/2006JA011897.

Geller, M. A., and L. Gong (2010), Gravity wave kinetic, potential, and vertical fluctuation energies as indicators of different frequency gravity waves, *J. Geophys. Res.*, *115*, D11111, doi:10.1029/2009JD012266.

González-Galindo, F., F. Forget, M. A. López-Valverde, M. Angelats i Colli, and E. Millour (2009a), A ground-to-exosphere Martian general circulation model: 1. Seasonal, diurnal, and solar cycle variation of

thermospheric temperatures, *J. Geophys. Res.*, *114*, E04001, doi:10.1029/2008JE003246.

González-Galindo, F., F. Forget, M. A. López-Valverde, and M. Angelats i Colli (2009b), A ground-to-exosphere Martian general circulation model: 2. Atmosphere during solstice conditions—Thermospheric polar warming, *J. Geophys. Res.*, *114*, E08004, doi:10.1029/2008JE003277.

Gusev, O. A., and A. A. Kutepov (2003), Non-LTE gas in planetary atmospheres, in *Stellar Atmosphere Modeling*, *ASP Conf. Ser.*, vol. 288, edited by I. Hubeny, D. Mihalas, and K. Werner, pp. 318–330, Astron. Soc. of the Pac., San Francisco, Calif.

Haberle, R. M., et al. (1999), General circulation model simulations of the Mars Pathfinder atmospheric structure investigation/meteorology data, *J. Geophys. Res.*, *104*, 8957–8974.

Hartogh, P., A. S. Medvedev, T. Kuroda, R. Saito, G. Villanueva, A. G. Feofolov, A. A. Kutepov, and U. Berger (2005), Description and climatology of a new general circulation model of the Martian atmosphere, *J. Geophys. Res.*, *110*, E11008, doi:10.1029/2005JE002498.

Heavens, N. G., M. I. Richardson, W. G. Lawson, C. Lee, D. J. McCleese, D. M. Kass, A. Kleinboehl, J. T. Schofild, W. A. Abdou, and J. H. Shirley (2010), Convective instability in the Martian middle atmosphere, *Icarus*, *208*, 574–589, doi:10.1016/j.icarus.2010.03.023.

Hertzog, A., G. Boccara, R. A. Vincent, F. Vial and P. Cocqurez (2008), Estimation of gravity wave momentum flux and phase speeds from quasi-Lagrangian stratospheric balloon flights. Part II: Results from Vorcore campaign in Antarctica, *J. Atmos. Sci.*, *65*, 3056–3070.

Hide, R. (1969), Dynamics of the atmospheres of the major planets with an appendix on the viscous boundary layer at the rigid bounding surface of an electrically-conducting rotating fluid in the presence of a magnetic field, *J. Atmos. Sci.*, *26*, 841–853.

Hinson, D. P., R. A. Simpson, J. D. Twicken, G. L. Tyler, and F. M. Flasar (1999), Initial results from radio occultation measurements with Mars Global Surveyor, *J. Geophys. Res.*, *104*, 26,997–27,012.

Joshi, M. M., B. N. Lawrence, and S. R. Lewis (1995), Gravity wave drag in three-dimensional atmospheric models of Mars, *J. Geophys. Res.*, *100*, 21,235–21,245.

Joshi, M. M., B. N. Lawrence, and S. R. Lewis (1996), The effect of spatial variations in unresolved topography on gravity wave drag in the Martian atmosphere, *Geophys. Res. Lett.*, *23*, 2927–2930.

Kuroda, T., A. S. Medvedev, P. Hartogh, and M. Takahashi (2007), Seasonal changes of the baroclinic wave activity in the northern hemisphere of Mars simulated with a GCM, *Geophys. Res. Lett.*, *34*, L09203, doi:10.1029/2006GL028816.

Kuroda, T., A. S. Medvedev, P. Hartogh, and M. Takahashi (2009), On forcing the winter polar warmings in the martian middle atmosphere during dust storms, *J. Meteorol. Soc. Jpn.*, *87*, 913–921, doi:10.2151/jmsj.87.913.

Kutepov, A. A., O. A. Gusev, and V. P. Ogibalov (1998), Solution of the non-LTE problem for molecular gas in planetary atmospheres: Superiority of accelerated lambda iteration, *J. Quant. Spectrosc. Radiat. Transf.*, *60*, 199–220.

McCleese, D. J., et al. (2008), Intense polar temperature inversion in the middle atmosphere of Mars, *Nat. Geosci.*, *1*, 745–749, doi:10.1038/ngeo332.

McCleese, D. J., et al. (2010), Structure and dynamics of the Martian lower and middle atmosphere as observed by the Mars Climate Sounder: Seasonal variations in zonal mean temperature, dust, and water ice aerosols, *J. Geophys. Res.*, *115*, E12016, doi:10.1029/2010JE003677.

McDunn, T. L., S. W. Bougher, J. Murphy, M. D. Smith, F. Forget, J.-L. Bertaux, and F. Montmessin (2010), Simulating the density and thermal structure of the middle atmosphere (<80–130 km) of Mars using the MGCMMTGCM: A comparison with MEX/SPICAM observations, *Icarus*, *206*, 5–17.

McDunn, T., S. W Bougher, A. Kleinböhl, and F. Forget (2011), Polar warming in the Martian atmosphere: An analysis of data from modern spacecraft, paper presented at Fourth International Workshop on the Mars Atmosphere: Modelling and Observations, NASA, 8–11 February, Paris.

Medvedev, A. S., and P. Hartogh (2007), Winter polar warmings and the meridional transport on Mars simulated with a general circulation model, *Icarus*, *186*, 97–110.

Medvedev, A. S., and G. P. Klaassen (1995), Vertical evolution of gravity wave spectra and the parameterization of associated wave drag, *J. Geophys. Res.*, *100*, 25,841–25,853.

Medvedev, A. S., and G. P. Klaassen (2000), Parameterization of gravity wave momentum deposition based on nonlinear wave interactions: Basic formulation and sensitivity tests, *J. Atmos. Sol.-Terr. Phys.*, *62*, 1015–1033.

Medvedev, A. S., and G. P. Klaassen (2001), Realistic semiannual oscillation simulated in a middle atmosphere general circulation model, *Geophys. Res. Lett.*, *28*, 733–736.

Medvedev, A. S., G. P. Klaassen, and S. R. Beagley (1998), On the role of an anisotropic gravity wave spectrum in maintaining the circulation of the middle atmosphere, *Geophys. Res. Lett.*, *25*, 509–512.

Medvedev, A. S., E. Yiğit, and P. Hartogh (2011), Estimates of gravity wave drag on Mars: Indication of a possible lower thermospheric wind reversal, *Icarus*, *211*, 909–912, doi:10.1016/j.icarus2010.10.013.

Nakajima, T., and M. Tanaka (1986), Matrix formulations for the transfer of solar radiation in a plane-parallel scattering atmosphere, *J. Quant. Spectrosc. Radiat. Transfer*, *35*, 13–21.

Nakajima, T., M. Tsukamoto, Y. Tsushima, A. Numaguti, and T. Kimura (2000), Modeling of the radiative processes in an atmospheric general circulation model, *Appl. Optics*, *39*(N27), 4869–4878.

Parish, H. F., G. Schubert, M. P. Hickey, and R. L. Walterscheid (2009), Propagation of tropospheric gravity waves into the upper atmosphere of Mars, *Icarus*, *203*, 28–37, doi:10.1016/j.icarus.2009.04.031.

Théodore, B., E. Lellouch, E. Chassefiere, and A. Hauchecorne (1993), Solstitial temperature inversions in the Martian middle atmosphere: Observational clues and 2–D modeling, *Icarus*, *105*, 512–528.

Tolson, R. H., G. M. Keating, G. J. Cancro, J. S. Parker, S. N. Noll, and B. L. Wilkerson (1999), Application of accelerometer data to Mars Global Surveyor aerobraking operations, *J. Spacecraft Rockets*, *36*, 323–329.

Tolson, R. H., G. M. Keating, B. E. George, P. E. Escalera, M. R. Werner, A. M. Dwyer, and J. L. Hanna (2002), Application of accelerometer data to Mars Odyssey aerobraking and atmospheric modeling, *J. Spacecraft Rockets*, *42*, 435–443.

Vadas, S. L., and D. C. Fritts (2005), Thermospheric responses to gravity waves: Influences of increasing viscosity and thermal diffusivity, *J. Geophys. Res.*, *110*, D15103, doi:10.1029/2004JD005574.

Withers, P. (2006), Mars Global Surveyor and Mars Odyssey accelerometer observations of the Martian upper atmosphere during aerobraking, *Geophys. Res. Lett.*, *33*, L02201, doi:10.1029/2005GL024447.

Yiğit, E., and A. S. Medvedev (2009), Heating and cooling of the thermosphere by internal gravity waves, *Geophys. Res. Lett.*, *36*, L14807, doi:10.1029/2009GL038507.

Yiğit, E., and A. S. Medvedev (2010), Internal gravity waves in the thermosphere during low and high solar activity: Simulation study, *J. Geophys. Res.*, *115*, A00G02, doi:10.1029/2009JA015106.

Yiğit, E., A. D. Aylward, and A. S. Medvedev (2008), Parameterization of the effects of vertically propagating gravity waves for thermosphere general circulation models: Sensitivity study, *J. Geophys. Res.*, *113*, D19106, doi:10.1029/2008JD010135.

Yiğit, E., A. S. Medvedev, A. D. Aylward, P. Hartogh, and M. J. Harris (2009), Modeling the effects of gravity wave momentum deposition on the general circulation above the turbopause, *J. Geophys. Res.*, *114*, D07101, doi:10.1029/2008JD011132.

E. Becker, Leibniz Institute of Atmospheric Physics, Schloss-Str. 6, D-18225 Kühlungsborn, Germany. (becker@iap-kborn.de)

P. Hartogh and A. S. Medvedev, Max Planck Institute for Solar System Research, Max-Planck-Str. 2, D-37191 Katlenburg-Lindau, Germany. (hartogh@mps.mpg.de; medvedev@mps.mpg.de)

E. Yiğit, Center for Space Environment Modeling, Department of Atmosphere, Oceanic and Space Sciences, University of Michigan, 1429 Space Research Bldg., 2455 Hayward St., Ann Arbor, MI 48109-2143, USA. (erdal@umich.edu)